Acta Materialia 288 (2025) 120854

Contents lists available at ScienceDirect

Acta Materialia

journal homepage: www.elsevier.com/locate/actamat

Full length article

# Helium nano-bubbles in copper thin films slows down creep under ion irradiation

Nargisse Khiara [a], Michaël Coulombier [c], Jean-Pierre Raskin [d], Yves Bréchet [b], Thomas Pardoen [c,e], Fabien Onimus [a,*]

[a] Université Paris-Saclay, CEA, Service de Recherche en Matériaux et procédés Avancés, 91191, Gif-sur-Yvette, France
[b] Materials science department, Monash University, Clayton Campus, Wellington Road, Clayton Victoria 3800, Australia
[c] Institute of Mechanics, Materials and Civil Engineering, UCLouvain, Place Sainte Barbe 2 L5.02.02, 1348, Louvain-la-Neuve, Belgium
[d] Institute of Information and Communication Technologies, Electronics and Applied Mathematics, UCLouvain, Place du Levant 2 L5.04.04, 1348, Louvain-la-Neuve, Belgium
[e] WEL Research Institute, avenue Pasteur, 6, 1300 Wavre, Belgique

ARTICLE INFO

*Keywords:*
Creep
Irradiation
Copper
Helium bubbles
Small-scale testing

ABSTRACT

Neutron irradiation of structural materials in nuclear applications is accompanied with a variety of microstructural changes including the generation of helium nano-voids at high doses. When operating under stress, irradiation creep is taking place, leading to change of dimensions of components, as well as relaxation of the springs or screw torque. These distortions may have important implications on the performance of the nuclear reactor. Irradiation creep is particularly complicated to investigate and the link between creep rate and microstructure remains partly elusive. Ultra-miniaturized testing of thin films makes possible the use of ion irradiation and implantation methods to emulate the effect of in-reactor neutron irradiation. Here, on-chip tests on freestanding copper films reveal much slower irradiation creep of helium implanted layers compared with non-implanted copper, with or without ion irradiation hardening prior to testing. This enhanced resistance to creep is due to the presence of the high density of helium bubbles, as evidenced by transmission electron microscopy, that impede dislocation glide and climb. A unified elementary model for moderate to high stress creep under irradiation is proposed showing that the creep law for the studied range of stress primarily depends on the yield strength which increases with helium bubbles.

## 1. Introduction

Structural and cladding materials used for nuclear applications, such as fission and fusion reactors, undergo intense neutron irradiation during operation that induces both a degradation of the mechanical properties and in-reactor deformation of the components. The dimensional instability of the components may have important implications on the performance of nuclear reactors. The evolution of the distortions must therefore be properly characterized, understood and predicted.

Deformation under irradiation of materials can be categorized into three different phenomena at the macroscopic scale: (i) irradiation induced swelling, (ii) irradiation induced growth, and (iii) irradiation creep. Irradiation induced swelling consists of an isotropic volume increase under irradiation without any applied stress. Irradiation induced growth is an anisotropic deformation at constant volume under irradiation without applied stress. Irradiation creep occurs under simultaneous applied stress and irradiation. Irradiation creep is the accumulation of viscoplastic strain over time, activated by the neutron flux, at constant volume. It takes place at moderate temperature for which thermal creep is negligible [1,2]. In the context of nuclear materials, thermal creep would be the usual viscoplastic deformation phenomenon activated by applied stress and temperature. The common method to study irradiation creep consists of conducting in-reactor experiments using for instance pressurized tubes, tensile specimens, bent beams, or helical springs [3,4]. This type of experiments requires long durations and leads to specimen activation.

An alternative to in-reactor experiments is to switch to light or heavy ion irradiation to accelerate testing and to reduce the amount of activated material waste. However, the low penetration depth of ions compared to neutrons must be taken into account when setting up the

* Corresponding author.
*E-mail address:* fabien.onimus@cea.fr (F. Onimus).

https://doi.org/10.1016/j.actamat.2025.120854
Received 27 August 2024; Received in revised form 27 January 2025; Accepted 19 February 2025
Available online 21 February 2025
1359-6454/

test. In order to characterize the irradiation creep behavior it has been proposed to use large scale specimens but with a very thin thickness (typically 50 to 100 μm) adapted to specific test rig, coupled with high energy light ion beam (helium ions or protons) [5–10]. Heavy ions have been used, as well, to reach higher damage dose within short duration. In this case, the specimens must be even thinner, typically between 1 μm down to 100 nm. Various original setups, using small-scale testing methods, have been proposed to measure the strain rate under controlled applied stress on such small specimens. Some designs are based on micro or nano-pillars positioned into the ion beam [11–15]. Other setups rely on free-standing films. For instance, Tai et al. [16,17] adapted a thin film bulge test method for this purpose. Lapouge et al. [18,19] developed an on-chip MEMS-based method in which a free-standing thin film is pulled in tension by an actuator beam. These alternative methods have already provided new insights about the irradiation creep behavior of metals. As an example, the work of Lapouge et al. [19] showed that for pure copper, the stress dependence of the irradiation creep strain rate follows a power law with a high stress exponent between 4 and 5 in agreement with in-reactor macroscopic tests under neutron irradiation. However, many aspects related to the irradiation creep behavior still remain unknown and could be investigated relatively easily, at least in principle, using these nanomechanics-based alternative techniques.

In a nuclear reactor, inelastic transmutation reactions sometimes occur in addition to the creation of point defects inside displacement cascade resulting from elastic collisions with fast neutrons. In some materials, such as materials containing nickel, these transmutation reactions lead to the generation of helium. The creation of helium atoms inside the material has several potentially detrimental effects such as enhanced swelling or embrittlement. It can also affect the irradiation creep behavior. However, only a limited number of studies were performed to investigate the impact of helium and helium nano-voids on irradiation creep. In-reactor experiments conducted on austenitic stainless steels indicated that, in the case of a high He/dpa ratio (dpa stands for displacement per atom) and a low neutron flux, the irradiation creep rate (per dpa) is larger compared to irradiation under a lower He/dpa ratio and a higher neutron flux [20]. However, when looking into a wider database, Grossbeck *et al.* [21] indicate that there is little or no effect of helium on irradiation creep. Later, Garner *et al.* [22], when analyzing in detail various experimental results, found an enhancement of the irradiation creep rate due to helium (He) generation. This effect was further modeled by Woo and Garner [23]. In order to better understand this effect, Atkins and McElroy [24] performed irradiation creep experiments using 3.7 MeV protons on 316L stainless steel tensile specimen pre-implanted with He ions. The pre-implantation was performed with 15 MeV He ions under stresses of 10 or 100 MPa at 1, 12 and 50 atomic ppm (part per million) of He leading to an irradiation damage up to 1 dpa. The irradiation creep compliance was then determined during a subsequent proton irradiation. The authors found a reduction of the irradiation creep compliance (i.e. lower creep rate for a given applied stress) with higher He concentration. Atkins and McElroy [24] suggested that the reduction in irradiation creep compliance with increased He content is due to the increase in bubble density that tends to harden the material. More recently, irradiation creep experiments have been conducted under He ion beam on various ferritic steels [6–8]. However, in these experiments it was not possible to distinguish between the effect of the irradiation damage only and the effect of He implantation.

The objective of the present study is to further explore the influence of He on the irradiation creep of metals. The goal is to extract quantitative data, unravel the irradiation creep mechanisms and unify the results with a physics-based model. For this purpose, following the work of Lapouge *et al.* [18,19], thin copper films fabricated by physical vapor deposition process have been implanted with 0.86% He atoms. These films have been subjected to simultaneous heavy ion irradiation and tensile loading, using the on-chip MEMS-based test method [18,19], and the irradiation creep rate has been compared with reference specimens with no He and with or without irradiation hardening prior to testing. Moreover, TEM observations were carried out after He implantation and after irradiation creep testing on thin foils taken out of the copper films.

## 2. Materials and experimental methods

Cu films are processed by Physical Vapor Deposition (PVD) electron evaporation with 99.999% purity [18,19]. Pure copper has been chosen as a model material for face-centered cubic (FCC) metals and alloys, which is the case for austenitic stainless steels widely used as nuclear structural material. Furthermore, copper and copper alloys play a key role in the design of fusion reactors, for instance for the mono-block elements [25], owing to a high thermal conductivity. Before deposition on the silicon wafer, a 3 nm-thick titanium layer is evaporated to ensure good adhesion with the substrate. The thickness of the Cu films is equal to ~500 nm. After deposition, annealing at a temperature of 150°C is imposed during 30 minutes, under reducing atmosphere (Ar, $H_2$) in order to prevent oxidation, to stabilize the microstructure and to increase the grain size. The resulting in-plane grain size is equal to ~500 nm, leading thus to an equiaxed morphology. The film also exhibits a strong {111} fiber texture (see later in Fig. 3a).

The experimental setup used to deform the Cu films is based on the UCLouvain MEMS-based on-chip mechanical testing method. The principle of the method is briefly recalled hereafter, supported by Fig. 1. More details can be found in [26–29]. Several layers are deposited successively on a Si wafer and patterned by photolithography and etching processes using clean-room facilities. An amorphous silicon nitride – $Si_3N_4$ - layer is deposited first by Low Pressure Chemical Vapor Deposition (LPCVD) on the silicon substrate at a temperature of 790°C. This layer has a thickness of 100 nm and exhibits a mismatch strain of $\varepsilon_a^{mis}$ = -0.0033 (the negative sign means that the film would contract if released and that the residual stress is thus tensile). $Si_3N_4$ has an isotropic linear elastic response and will act as the actuator. The actuator layer is patterned into a long beam with a slight taper using dry etching ($SF_6$ plasma followed by $CHF_3$ and $O_2$ plasma). The Cu specimen layer is deposited next and patterned by lift-off process into a classical dogbone tensile specimen shape, including an overlap with the actuator beam. Cursors are patterned on both sides of the overlap between the specimen and actuator, as shown in Fig. 1b. The displacement ($u$) imposed to the specimen is measured after release in a scanning electron microscope (SEM) based on the displacement of cursors with respect to a reference position. The release process of the test structure is performed using $XeF_2$ dry etching of the silicon substrate. After release, mechanical equilibrium is attained through elastic unloading of the actuator and loading of the specimen, see Fig. 1a, which deforms in a purely elastic manner for short actuators and in the plastic regime with longer actuators.

The true uniaxial strain and stress in the specimen can be deduced from the measurement of the displacement ($u$) as

$$\varepsilon = \ln\left(\frac{L_0 + u}{L_0}\right) - \varepsilon^{mis}, \tag{1}$$

$$\sigma = \frac{S_a E_a}{S_0}\left[\ln\left(\frac{L_{a,0} - u}{L_{a,0}}\right) - \varepsilon_a^{mis}\right]\exp(\varepsilon) \ . \tag{2}$$

This requires knowing the magnitude of the Young's modulus of the actuator ($E_a$), the mismatch strain of the actuator ($\varepsilon_a^{mis}$) and of the specimen ($\varepsilon^{mis}$). The mismatch strains are determined by measuring the contraction of free beams, and by cross-checking the values using the Stoney method providing the residual stress in the film out of which the mismatch strain can be extracted knowing the Young's modulus, see e.g. [30]. The geometry of the test structure is given by the initial length of the specimen ($L_0$), the cross-section of the specimen ($S_0$), the initial length of the actuator ($L_{a,0}$) and the cross-section of the actuator ($S_a$).

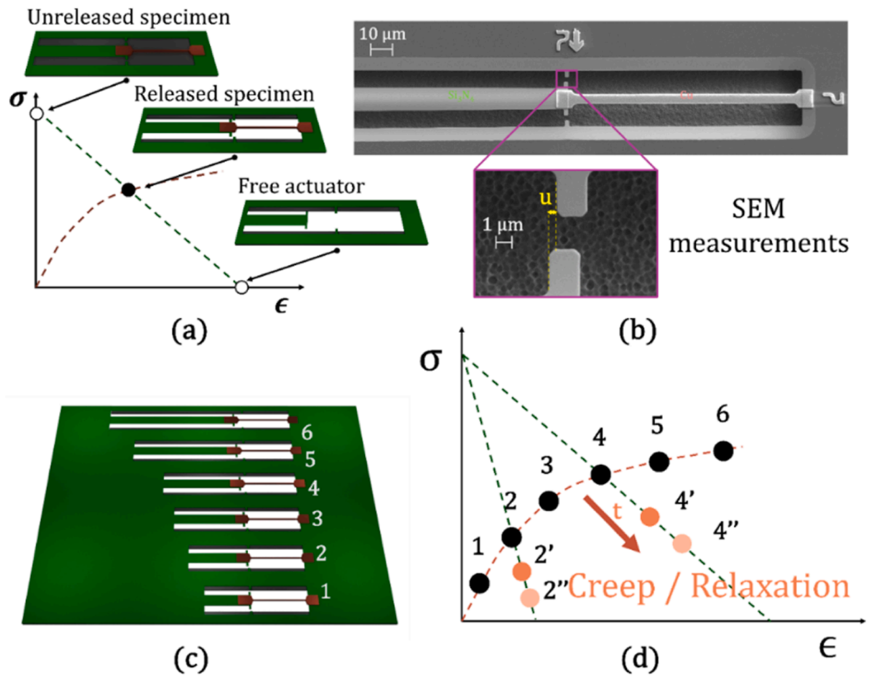


**Fig. 1.** Principle of the on chip tensile testing method. (a) Mechanical equilibrium between actuator and specimen after release. (b) SEM micrograph of a single elementary test structure with magnification of the zone with the cursors used to determine the applied displacement. (c) Schematic of a series of test structures with different actuator lengths. (d) Principle of the construction of the stress-strain response including the evolution under creep/relaxation with time for different actuator lengths.

The corresponding stress and strain at mechanical equilibrium provides a single point in the stress-strain diagram. Fig. 1c and 1d and Fig. 2a and 2b illustrate that different test structures, with various actuator lengths, lead to different levels of loading, out of which one can construct the full stress-strain response of the material. The stress-strain response is thus the result of testing many specimens, hence delivering a statistically meaningful averaging of the mechanical tensile response of the Cu films. In the case of a visco-plastic behavior, the equilibrium working point evolves as the actuator keeps relaxing and the specimen elongating with time as illustrated schematically in Fig. 1d. This leads to a loading condition in between pure creep and pure relaxation.

The specimens have been implanted with He and/or irradiated with Cu ions. Fig. 2d shows that the masking device has been designed to protect the actuators during irradiation/implantation, as described in detail in reference [18]. It consists in a stainless steel foil accurately positioned and aligned in front of the actuators, at the actuator-specimen overlap, so that only the specimen gauge length is exposed to the ion beam, see Fig. 2b and 2c. In this context, a specific set of photolithography masks has been designed so that all test structures are compatible with the masking device and can be tested for creep in a single irradiation, see Fig. 2a. The specimens used have a length equal to 50, 100, or 400 µm and widths of 1.5, 2.5, or 4 µm. The actuators have a width equal to 12 µm and lengths that vary between 50 and 1500 µm. The structures are gathered by specimen widths, each group is divided into three sets depending on specimen length. Each set contains 30 test structures with the same specimen width and length but increasing actuator length, resulting in to a pan-pipe-type geometry (Fig. 2a). Therefore, in total, there are 270 structures (3 × 3 × 30). The test structures used for the irradiation study are duplicated (mirrored) so that two identical experiments are performed simultaneously. Hence, a test structure can be irradiated while its mirror test structure is protected by the stainless steel foil. This mirror test structure thus acts as control specimen. This allows for a direct comparison between the mechanical behavior with and without irradiation.

First, some specimens have been implanted with He atoms (at the MOSAIC/IJCLab facility) by imposing four successive He energies (20 keV: $0.5 \times 10^{16}$, 40 keV: $1.0 \times 10^{16}$, 80 keV: $0.75 \times 10^{16}$, 100 keV: $1.6 \times 10^{16}$ in ions/cm$^2$) in order to obtain a nearly homogeneous implantation profile over the thickness of the specimen (Fig. 3d). Implantation and damage profile computations are performed with the software SRIM 2013 [31–33] in the Quick Calculation (Kinchin Pease) mode as recommended in [32,33], using a displacement energy of 30 eV [34,35]. It must be pointed out that early works found lower values for the displacement energy equal to 22 eV [36] or 16–19 eV [37]. Recently, some authors used [38] a value of 25 eV for the displacement energy. In the previous study [18,19] full damage cascade mode was used with displacement energy of 25 eV leading to a damage rate approximately three times higher.

The total fluence reached is $3.85\ \times 10^{16}$ ions/cm$^2$ which corresponds to approximately 0.86% (atomic percent) of implanted He atoms when averaged over a thickness of 500 nm. This He implantation induces an average damage dose of 0.70 dpa over the thickness (Fig. 3d). In order to distinguish between the effect of the He implantation only and the effect of the irradiation damage, other specimens have been irradiated with 1.2 MeV Cu ions up to a fluence of $4\ \times 10^{14}$ ions/cm$^2$ which corresponds to a damage dose of 0.66 dpa averaged over the thickness of the specimen. The computed irradiation profile is shown in Fig. 3b. The same damage profile has been computed using the software IRADINA [39] with the same parameters and using the "SRIM like" mode. The same profile is obtained using the different software. As for a former study [18,19] a tilt of the sample of 7° has been introduced in order to avoid any channeling effect. The mechanical behavior of these two types of specimens has then been studied and compared with unirradiated specimens referred to as "pristine Cu" in the following.

The test structures are released after He implantation or Cu irradiation. The displacements $u$ are measured in a SEM, on the same day of the release, at least 30 minutes after release. During this time, the test structures have already relaxed by a small amount. The stresses upon release are thus slightly underestimated and the strains slightly overestimated. The mismatch strain of the sample ($\varepsilon^{mis}$) is evaluated for each specimen, by forcing the linear fit of the points in the elastic domain to go through the origin of the stress-strain diagram. The mismatch strain

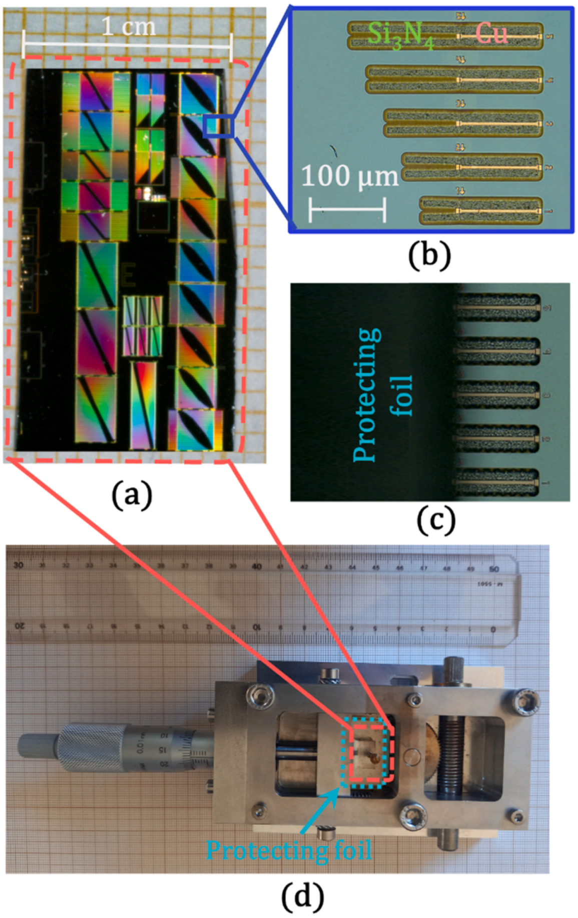


**Fig. 2.** Set up for on-chip irradiation creep experiments: (a) As-fabricated test structures. (b) Test structures observed with optical microscopy showing the actuators with various lengths and the specimens. (c) Same test structures with the foil aligned which protects the actuators. (d) Device used for accurately positioning the protecting foil above the SiN actuators.

($\varepsilon^{mis}$) for pristine (unirradiated) Cu, 0.66 dpa irradiated Cu and 0.86% at. He implanted Cu are, respectively, equal to: -9.3 $\times$ $10^{-4}$, -9.8 $\times$ $10^{-4}$ and $+8.7$ $\times$ $10^{-4}$. This shows that irradiation does not affect the mismatch strain or residual stress, while the He implantation drastically modifies the residual stress from tension to compression in the Cu film. The Young's modulus of the Cu film is equal to $E_{Cu} = 110$ GPa and the Young's modulus of the actuator material is equal to $E_a = 250$ GPa. Both were measured by nano-indentation [30] which provides more accurate and reliable Young's modulus than the on-chip test for the specific geometries tested in the context of this study.

The irradiation creep response is determined by sequentially irradiating the specimen with a dose increment and measuring the displacement right after. More precisely, the displacement of specimens released several days before the irradiation creep test starts (8 days before for pristine Cu and He implanted Cu, 42 days before for the layer irradiated with Cu ions) is measured again by SEM in order to determine possible creep deformation accumulation out of irradiation. Then, these specimens are subsequently irradiated using 1.2 MeV Cu ions (on the MOSAIC/IJCLab facility) in four successive irradiation steps. The four successive doses (1/3, 2/3, 2/3 and 1 dpa) lead to a total dose of 8/3 dpa. Between each of these irradiation steps, the specimens are taken out of the irradiation facility and the displacements are measured by SEM. Simultaneously, control samples are also measured. As explained previously, from the measurements of the displacement ($u$) before and after irradiation, the specimen strain and stress before ($\varepsilon_{i-1}$ and $\sigma_{i-1}$) and after ($\varepsilon_i$ and $\sigma_i$) an irradiation step are deduced. As the stress relaxes during an irradiation step, it is necessary to evaluate a representative mean stress taken as the average of the stress before ($\sigma_{i-1}$) and after ($\sigma_i$) the irradiation step as:

$$\overline{\sigma}_i = \frac{(\sigma_i + \sigma_{i-1})}{2}\ . \tag{3}$$

The visco-plastic strain increase ($\Delta\varepsilon_i^{vp}$) during the irradiation step ($i$) is computed as the total strain increase minus the change of the elastic strain (here a decrease) due to the stress relaxation (Eq. 4):

$$\Delta\varepsilon_i^{vp} = (\varepsilon_i - \varepsilon_{i-1}) - \frac{(\sigma_i - \sigma_{i-1})}{E_{Cu}}. \tag{4}$$

The irradiation creep strain rate is deduced as a function of the irradiation dose increase during the step ($\Delta D_i$ in dpa) as $\Delta\varepsilon_i^{vp}/\Delta D_i$ and then related to the mean stress ($\overline{\sigma}_i$).

In addition to these small-scale mechanical tests, transmission electron microscopy (TEM) characterizations have been conducted on thin foils taken out by focus ion beam (FIB) milling, using a Helios 650 NanoLab FEI-focused ion beam, from the thin Cu films. The thin foils were taken in the cross-section of the films, with the length of the TEM thin foil along the length of the beam. A conventional process implying platinum deposition then gallium ion milling has been used.

## 3. Results

### 3.1. Plastic behaviour after irradiation or implantation

Fig. 4 shows the true stress – true strain response of the unirradiated specimens, of the specimens irradiated with Cu ions and of the specimens implanted with He ions. The yield stress at 0.2% is approximately equal to $\sigma_{0.2\%}^{pristine} = 250$ MPa, $\sigma_{0.2\%}^{Cu} = 380$ MPa and $\sigma_{0.2\%}^{He} = 500$ MPa, for respectively the pristine Cu (unirradiated), the irradiated Cu with Cu ions and the He implanted Cu. The He implanted Cu specimen has the highest yield stress, followed by the irradiated Cu, then the pristine Cu. First, this demonstrates that 0.66 dpa irradiation induces significant hardening. Second, for similar damage level of 0.7 dpa, 0.86% at. He implantation induces more hardening compared with Cu ion irradiation. Moreover, He implantation induces a significant reduction of the ductility. Note that for the irradiated Cu the data does not cover the entire stress-strain response up to the fracture point because the actuator beams were not sufficiently long and wide to impose the necessary level of deformation. It will be shown later that the hardening due to irradiation damage is attributed to the formation of numerous stacking fault tetrahedra (SFT) under irradiation and that the hardening due to He implantation is attributed to the formation of nanometric He-bubbles.

### 3.2. Mechanical behavior under irradiation

The variation of the strain incrementally measured during the irradiation experiments is given as a function of time in Fig. 5. Fig. 5a shows the behavior of the pristine Cu film and Fig. 5b shows the behavior of the 1% He implanted Cu. The vertical red rectangles indicate the irradiation steps with the corresponding damage dose. Each symbol corresponds to a specific test structure. The value given in the legend is the ratio between the actuator length and the specimen length $L_a/L_{Cu}$ of the corresponding test structure. Fig. 5a and 5b show that the deformation does not change without irradiation. The two steps without irradiation correspond to the previous night and the night in the middle of the experiment. This can also be confirmed by looking at the control specimens in Fig. 5c and 5d that are protected by the stainless steel foil. On the other hand, strain significantly increases during the 4 irradiation steps. This is the signature of the irradiation creep phenomenon of interest in this study. Note that the strain is larger when the ratio $L_a/L_{Cu}$ is larger, which is consistent with the effect of the actuator length on the applied stress, the applied load being larger when the actuator length is

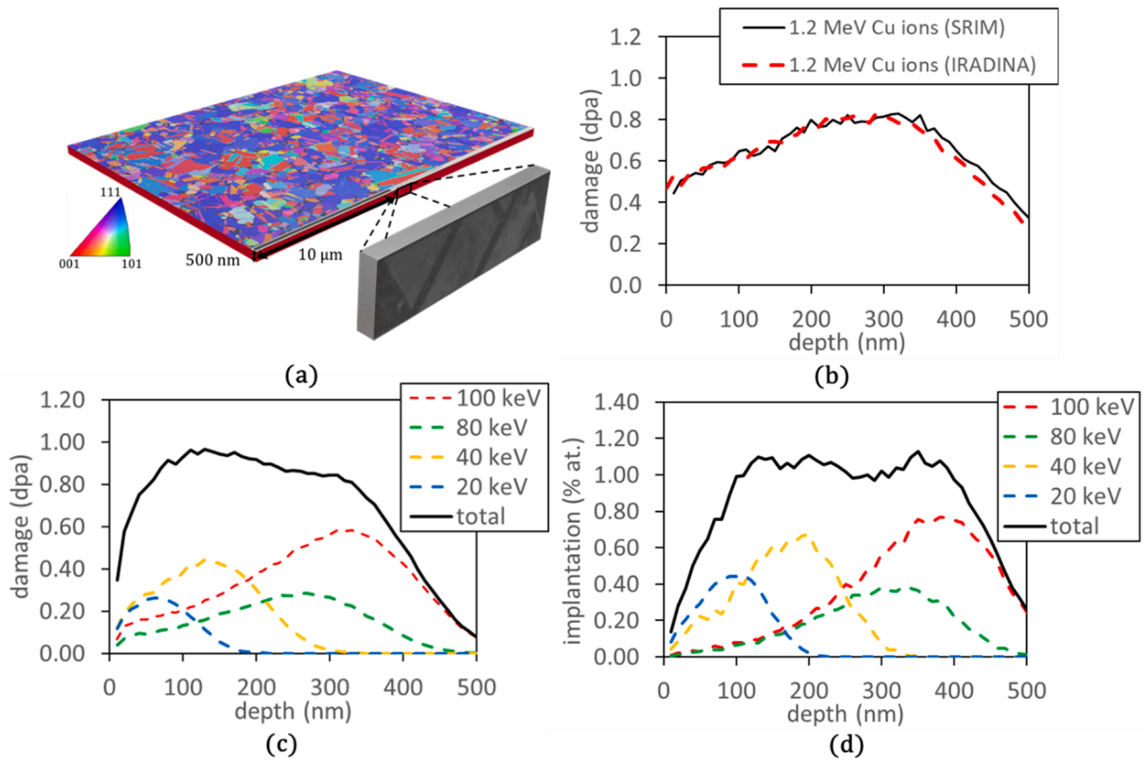


**Fig. 3.** (a) EBSD map of the 500 nm thick Cu foil. The corresponding colors are given in the Inverse Pole Figure. A TEM micrograph of the cross-section of the foil is also shown. (b) Damage profile in the Cu film calculated with the SRIM 2013 software using the Quick Calculation mode and 30 eV as displacement energy for a fluence of $4 \times 10^{14}$ ions /cm$^2$. (c) He implantation profile, given in atomic % computed with the SRIM 2013 software using Quick Calculation mode and 30 eV as displacement energy. The black continuous line shows the overall He concentration. (d) Damage profile obtained during He implantation. The black continuous line shows the overall damage profile.

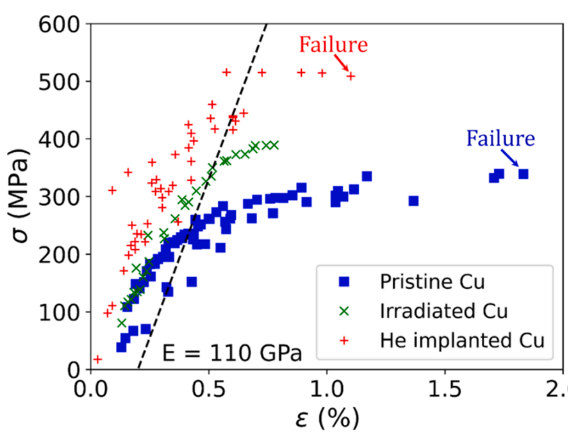


**Fig. 4.** True stress – true strain response of Cu after irradiation or implantation extracted from the release of on-chip test structures. The measurements are performed the same day of the release.

longer.

Fig. 6 shows the stress-strain evolution under irradiation of the (a) pristine and (b) He-implanted specimens. One should be careful not misinterpreting these data as stress-strain curves because they belong to specimens having a different creep history associated to different imposed initial levels of stress. As described schematically in Fig. 1, under irradiation, the stress decreases and the strain increases, following straight lines that connect the points related to the same specimen. SEM observations reveal that the test structures that have undergone irradiation creep deformation remain homogeneous with no sign of localization or failure under irradiation.

The irradiation creep strain increments associated to the increments of irradiation dose ($\Delta\varepsilon_i^{vp}/\Delta D_i$) are computed and plotted in Fig. 7a as a function of the mean stress ($\overline{\sigma}_i$) during the corresponding irradiation step. The result of a power law fit is also shown in Fig. 7a. The hatched area around each curve represents the impact of an error of ± 5% on the actuator thickness which is the main uncertainty factor in the experimental data reduction. The creep strain rate follows a power law with a stress exponent close to 4 for the three families of specimens. The corresponding multiplication pre-factors are equal to $2.12 \times 10^{-12}$, $1.32 \times 10^{-12}$, and $3.05 \times 10^{-13}$ MPa$^{-4}$ dpa$^{-1}$ for pristine Cu, irradiated Cu and He implanted Cu, respectively. This high stress exponent, equal to 4, is in good agreement with previous results obtained on Cu for moderate and high applied stresses [18,19,40,41].

Pristine Cu and pre-irradiated Cu exhibit similar behavior with relatively similar pre-factors. In order to further analyze these results, the points corresponding to the first irradiation step (0.33 dpa) of the initially unirradiated sample have been represented as filled light-blue squares in Fig. 7a and the points corresponding to the subsequent irradiation steps are represented as smaller filled dark-blue squares. The filled dark-blue squares align with the green points corresponding to the pre-irradiated sample. This indicates that the irradiation creep behavior after 0.33 dpa irradiation (under stress) is the same as the creep behavior after 0.66 dpa irradiation (without stress).

On the other hand, the creep rates of He implanted Cu films are much lower than pre-irradiated Cu, with one order of magnitude lower pre-factor in agreement with the experiments conducted by Atkins and McElroy [24], as further discussed in the next section.

In order to investigate the impact of the hardening on irradiation creep, a simple irradiation creep model based on dislocation glide assisted by irradiation is proposed. Thermodynamic and kinetics based models of dislocation glide [42–44], justify that the strain rate can be reasonably well related to a power law of the applied stress divided by

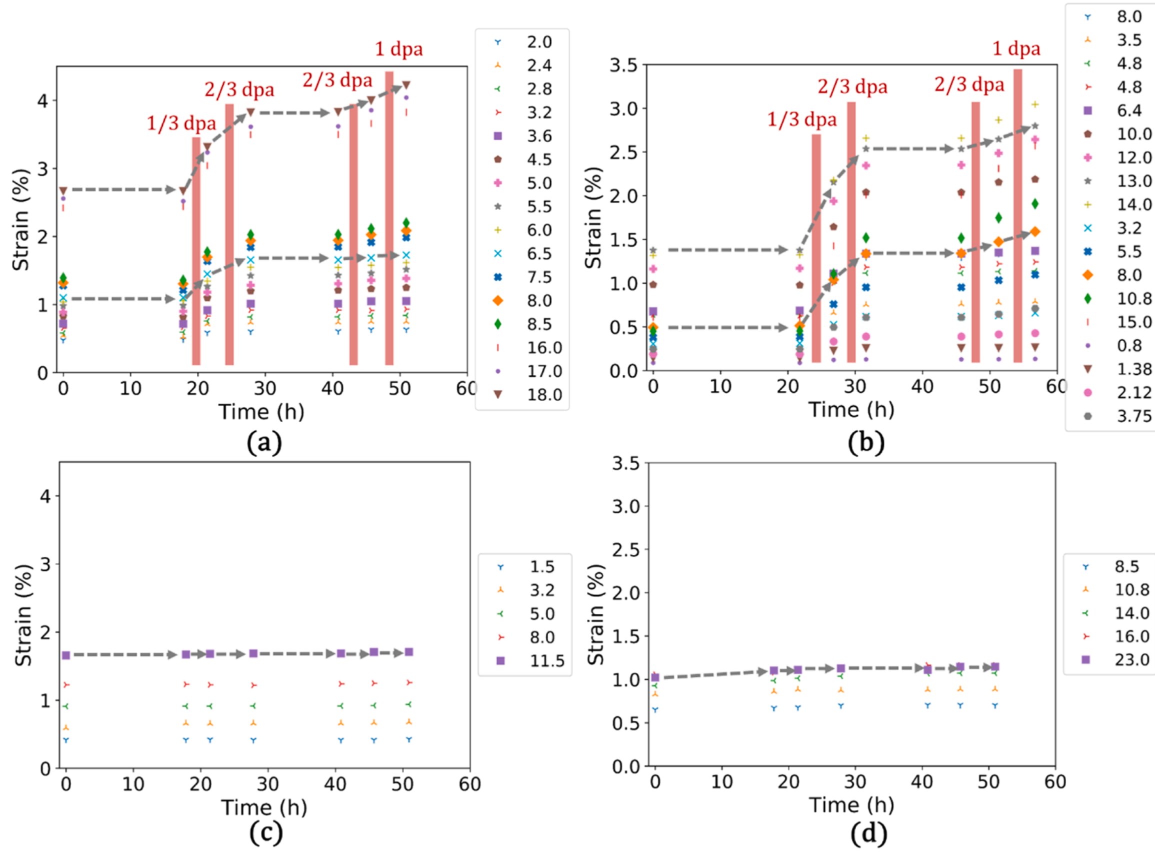


**Fig. 5.** Variation of the total strain as a function of time under irradiation for (a) the pristine specimen and (b) the He-implanted specimen. The irradiation sequences are shown as vertical red bars with the damage dose written above. Variation of the strain as a function of time out of the ion beam (control samples) for (c) the pristine specimen and (d) the He-implanted specimen. Dotted lines have been added to help the reader to follow the evolution of the strain of few test structures with time. The value given in the legend is the ratio between the actuator length and the specimen length $L_a/L_{Cu}$ of the corresponding test structure.

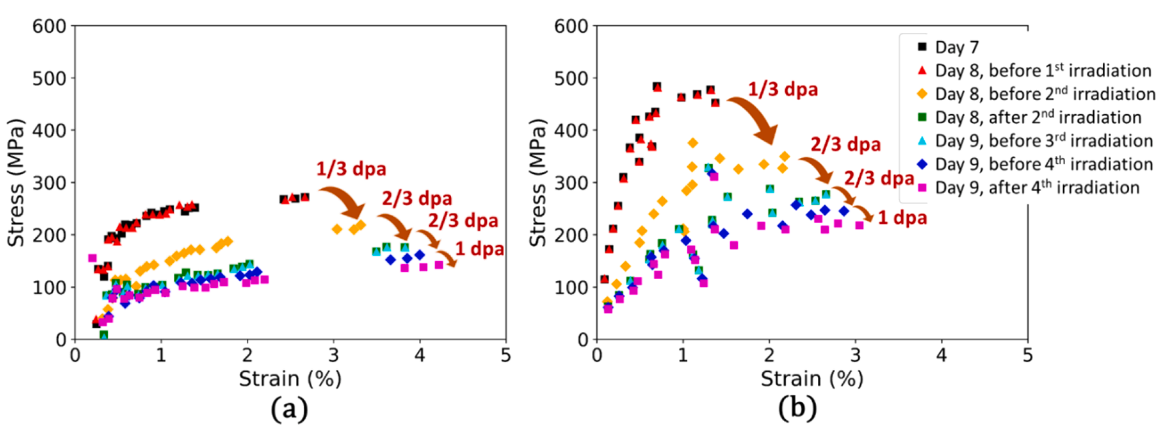


**Fig. 6.** (a) Stress-strain response under irradiation(conducted after release) of the pristine sample. The evolution of the curves is shown for each increment of the irradiation dose. (b) Stress-strain curves under irradiation (conducted after release) of the He-implanted sample showing the evolution of the curve for each increment of the irradiation dose.

the mechanical threshold stress that represents the resistance to dislocation glide. This mechanical threshold can be taken here as yield stress measured prior to irradiation creep, after the release of the specimens. Depending on the physically based model considered for creep controlled by dislocation glide, a stress exponent varying between 3 and 5 [45,46] has been proposed. A stress exponent of 4 is adopted in this work leading to

$$\frac{d\varepsilon^{vp}}{dD} = 0.087\left(\frac{\sigma}{\sigma_{0.2\%}}\right)^4 \tag{5}$$

with the pre-factor 0.087 dpa$^{-1}$adjusted to the get the best agreement with the experimental data. This identification was based on the following yield stress values for the different conditions. The yield stress of the pre-irradiated Cu ($\sigma_{0.2\%}^{Cu} = 380$ MPa), determined by the on-chip test method, is used for both the pre-irradiated Cu and the unirradiated

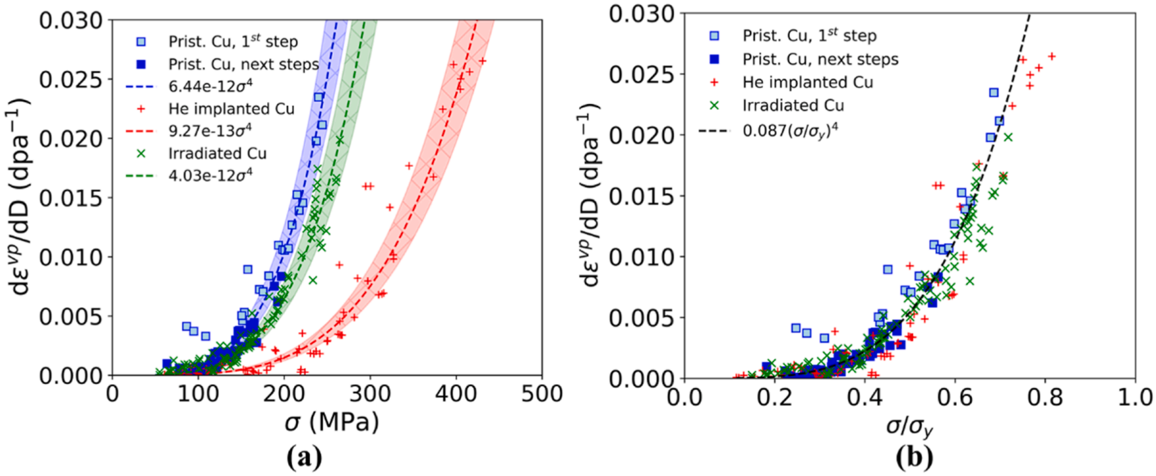


**Fig. 7.** (a) Variation the creep strain increment per dpa as a function of stress for pristine Cu, He-implanted Cu and irradiated Cu (all the steps are considered for the fitting of the pristine Cu). (b) The creep strain rate per dpa is represented as a function of the stress divided by the yield stress. The light blue points that correspond to the first irradiation step are not considered for the adjustment of the model.

(pristine) Cu, only considering the points obtained from the second irradiation steps, shown as smaller dark blue squares in Fig. 7b. The yield stress $\sigma_{0.2\%}^{1\%He} = 500$ MPa, also determined by the on-chip test, is used for the He implanted Cu. Fig. 7b shows conspicuous agreement between the model and experiments, leading to a single master curve. It is important to insist on that the model relies on a single tuning factor only. This indicates that the irradiation creep behavior at moderate stresses and low temperatures is essentially controlled by the magnitude of the yield stress for reasons that are discussed in the sequel.

### 3.3. Defect analysis before and after irradiation creep

The microstructure after 0.86% at. He implantation has been characterized by TEM, see Fig. 8a and 8b. The distribution of bubbles is

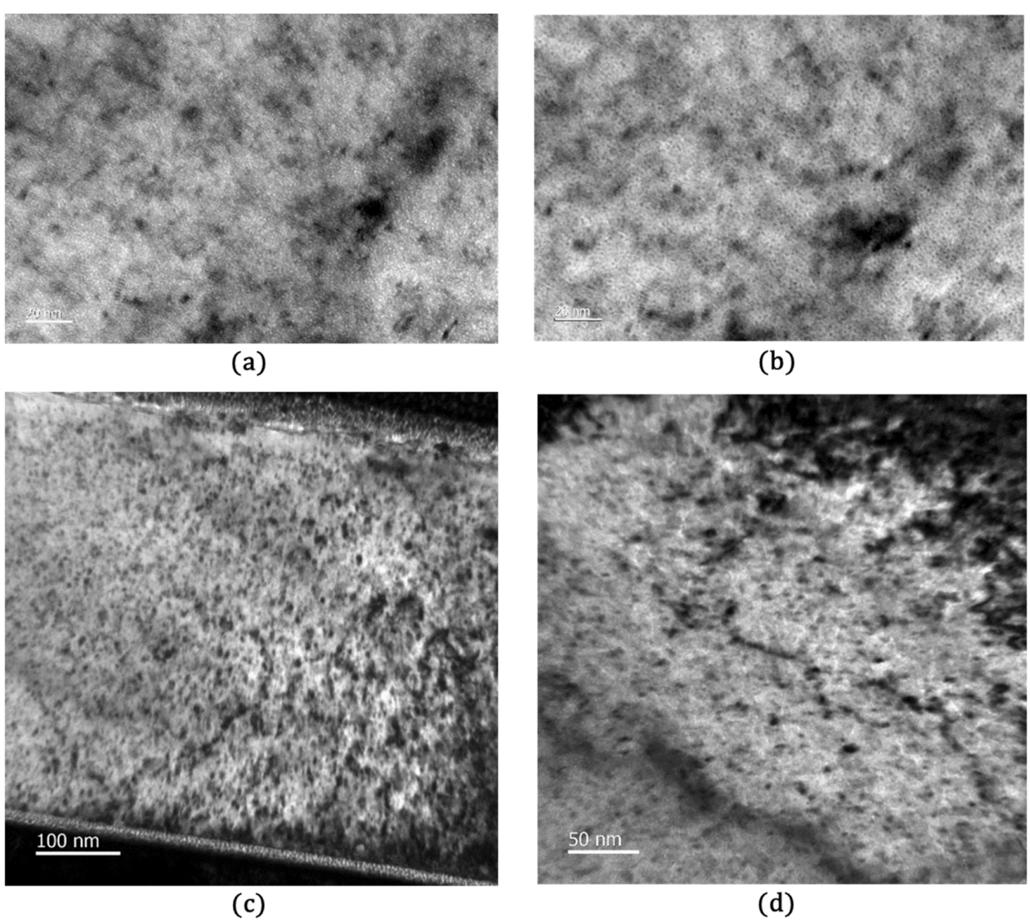


**Fig. 8.** (a,b) He bubbles observed using (a) underfocus conditions and (b) overfocus conditions; (c) jogged dislocations in the pristine Cu film after irradiation creep; (d) jogged dislocations in the He-implanted Cu film after irradiation creep.

homogenous with a diameter of $d \approx 0.9$ nm, estimated using the through focus technique [47,48]. This bubble size is in agreement with other values found in the literature [48–51]. From the knowledge of the He content (~1% at.) and bubble size ($d \approx 0.9$ nm), the bubble density is found to be close to $N = 1 \times 10^{25}$ m$^{-3}$ depending on the method used [48,49,51]. No bubble superlattice is observed at this damage level. The irradiated Cu microstructure was also previously analyzed [18]. It mainly consists of small SFT with density of $N = 2.5 \times 10^{23}$ m$^{-3}$ and mean size of $d = 2.5$ nm in agreement again with values found in the literature [52–55]. These SFT are sometimes difficult to detect depending on the thickness and quality of the thin foil. Often, only black dots can be distinguished which are either small SFT or small dislocation loops.

Thin foils prepared by FIB milling from Cu films after irradiation creep have been also characterized by TEM. In the pristine Cu (Fig. 8c) and He-implanted Cu (Fig. 8d) specimens, jogged dislocations are observed in the midst of numerous irradiation defects, SFT or bubbles. TEM analysis reveals very limited bubble growth, considering the accuracy of the measurement.

## 4. Discussion

The on-chip uniaxial tensile tests reveal the expected significant hardening of the ion irradiated and He implanted Cu films compared to unirradiated conditions. He implantation leads to a significantly larger hardening than Cu ion irradiation, even though the irradiation dose is almost identical, equal to 0.7 dpa and 0.66 dpa, respectively. The hardening of the Cu ion irradiated layer is attributed to the numerous stacking fault tetrahedra (SFT) produced under irradiation that impede dislocation glide [19,52,56,57]. The significant hardening of the He implantation is attributed to the high density of nano He bubbles that are very effective to impede dislocation glide [48,51,58]. The elementary hardening induced by these two types of defects can be approximately estimated by considering the dispersed barrier hardening model (DBH), see [59]. According to this model, the increase of yield stress $\Delta\sigma$ can be quantified by the following relationship

$$\Delta\sigma = \alpha(d) M \mu b \sqrt{Nd}, \tag{6}$$

where $M$ is the Taylor factor, $\mu$ is the shear modulus, $b$ is the Burgers vector, $d$ is the defect size and $N$ the defect density. The coefficient $\alpha(d)$ is characteristic of the strength of the obstacle, which depends on the type of obstacle and which is an increasing function of its size [59]. The influence of the obstacle size on the strengthening can be rationalized by using various models [59] such as the Bacon Kocks Scattergood (BKS) model [60–62] which is not considered here. The following values for the various parameters of the DBH model were selected: $M = 3.06$ [63], $\mu = 46$ GPa [51], $b = 0.256$ nm. The choice of $M$=3.06 is an upper bound value valid for a polycrystal with no crystallographic texture. The true value is not known, but probably smaller due to the lower constraint on plasticity of the present single-grain-over-the-thickness morphology, with marked crystallographic texture. Based on yield stresses measured on-chip and reported in Section 3.2 as well as the values of $d$ and $N$ reported in Section 3.3, Eq. (6) gives a coefficient $\alpha$ equal to $\alpha_{bubbles}^{on-chip} \approx 0.07$ for He-implanted Cu. This value is in good agreement with the value obtained by Wang *et al.* [50] from compression tests on nanopillars. Concerning Cu irradiated with Cu ions, the coefficient $\alpha$ associated to SFT is found to be equal to $\alpha_{SFT}^{on-chip} \approx 0.14$. This last value is not far from the value of 0.2 reported in the Supplementary Information of ref. [52].

The ratio between the strength coefficient for bubbles and for SFT is equal to $\alpha_{bubbles}^{on-chip}/\alpha_{SFT}^{on-chip} \approx 0.5$, independent of the parameters $M$, $\mu$, $b$ chosen. This ratio is discussed further in connection to the literature. If the model used above is correct and the experiments presented in this study valid and accurate, it leads to the conclusion that the hardening potential induced by a single bubble, smaller than 1 nm, would be close to half of the hardening induced by a 2 nm single SFT. The smaller hardening induced by individual bubble can be partly explained by the smaller size of the defect since $\alpha(d)$ decreases as the defect size decreases. Assuming that a bubble behaves similar to a cavity and that a SFT behaves similar to a Frank loop, our results can be compared with the analysis of Tan and Busby [59] where the hardening induced by cavities is compared to the hardening induced by Frank loops. The influence of obstacle size was clearly noticed by these authors. Furthermore, they found that a cavity with a diameter close to 1 nm induces a much lower hardening than a Frank loop with the same size which further consolidates our own finding.

The on-chip experiments performed under simultaneous irradiation and applied stress, conducted after the release of test structures, show significantly deformation during the irradiation steps. This is the evidence of the irradiation creep phenomenon. The analysis of the experiments shows that the irradiation creep strain rate of Cu follows a power law function of stress, with a high exponent close to 4. SEM observations reveal that during irradiation creep, the deformation shows no evidence of localization or failure. This means that even though up to 2% of extra creep deformation has been sometimes generated through irradiation creep, none of the on-chip test structures broke. This effect has already been noticed by Lapouge et al. [19]. Although no rate sensitivity analysis was performed here, this effect can be related to the large rate sensitivity that is accompanying the irradiation creep response. A high rate sensitivity stabilizes plastic localization and explains why some thin metallic films can be very ductile [64].

Different mechanisms are proposed in the literature to explain the irradiation creep phenomenon [1,2]. An important class of mechanisms implies the anisotropic redistribution under applied stress of the numerous point defects created by irradiation. In this class of mechanisms, the stress induces a preferential absorption of point defects by dislocations leading to anisotropic climb [65–68]. The influence of the applied stress on the preferential nucleation or growth of dislocation loops could also explain part of the deformation occurring under irradiation [69]. There are relatively few microscopic evidences of these mechanisms, as reviewed in [2,70]. Recently, experiments conducted in-situ inside a transmission electron microscope on pure aluminum [71] show that stress induced preferential absorption of point defects by dislocation loops is in fact very limited and would therefore have a negligible contribution to irradiation creep. However, stress induced preferential nucleation of loops is clearly observed. This last mechanism could therefore contribute to irradiation creep deformation but most probably in a limited way. Nevertheless, this class of mechanisms leads to a stress exponent equal to one and cannot explain the behavior revealed by the present experiments.

A second important class of mechanisms implies the glide of dislocations enhanced by climb due to the absorption of point defects by dislocations under irradiation [72]. This class of mechanisms, involving dislocation glide leads to a high stress exponent, typically higher than three. Again, there is yet no clear microscopic experimental evidence of this mechanism. Another glide-based mechanism has been recently observed in-situ inside TEM in pure Cu [73], and zirconium alloys [74], under simultaneous ion irradiation and tensile loading. This mechanism is based on the fact that ion irradiation, as for neutron irradiation, creates displacement cascades. If the displacement cascade falls on a pinning point, such as a junction with a loop, or with a SFT, the dislocation can be released and glide freely up to the next pinning point. This mechanism has been reproduced numerically using Molecular Dynamics simulations [75,76] and recently applied to irradiation creep modelling [77].

The fact the stress exponent determined by the on-chip experiments is close to 4 suggests that the active deformation mechanism involves dislocation glide. Such mechanism was already proposed in the literature to explain the high stress irradiation creep in Cu [40,78], as well as in other materials [78–80]. Furthermore, post-irradiation FIB samples for Cu and He implanted Cu showed evidence of jogged dislocations. These jogs probably result from simultaneous dislocation climb and glide under irradiation.

The fact that the irradiation creep behavior after 1/3 dpa irradiation is the same as the creep behavior after 2/3 dpa irradiation can be explained by the rapid stabilization of the microstructure under irradiation. Several authors found that the irradiation defect density saturates, at a small dose, lower than 0.1 dpa [25,81]. This justifies the fact that the irradiation creep behavior after the first irradiation step is found to be the same as for the pre-irradiated sample.

For the He-implanted Cu, we demonstrate that irradiation creep is reduced by the presence of He bubbles. This can be explained by the fact that bubbles act as obstacles for dislocation glide, thus leading to a reduced irradiation creep rate. The fact that a power creep law normalized by the yield stress describes very well the behavior of both pristine Cu and He-implanted Cu again suggests that the active mechanism is the dislocation glide assisted by climb or dislocation unpinning under displacement cascades.

From the previous findings, the highly non-linear relationship with stress and the dependence on the yield stress of the irradiation creep rules out the classical mechanism of point defect agglomeration as the major contributors to irradiation creep, at least in these conditions. The irradiation induced unpinning from pinning points, observed in situ under simultaneous loading and irradiation [73] and simulated using molecular dynamics simulations [76], seems to be the most probable mechanism, being operative for dislocation loops, SFT and He bubbles. It explains physically the possibility of a master curve for the irradiation creep rate when the stress is normalized by the yield stress, the main effect of He bubble being to add new obstacles to dislocation glide, and to increase the yield stress.

## 5. Conclusion

Freestanding thin Cu films pre-irradiated with Cu ions or implanted with He atoms have been loaded on chip in tension, and subjected to irradiation creep conditions with Cu ions. The main findings of this study are the following

- Cu film hardens under 0.66 dpa Cu ion by 50% as a result of the production of a high density of stacking fault tetrahedra impeding dislocation glide. The hardening is significantly higher, by 100%, when the Cu film is implanted with 0.86% He atoms inducing the formation of a very high density of nano bubbles that also impede dislocation glide.
- The modelling of the hardening induced by a single bubble smaller than 1 nm or a single 2 nm SFT shows that the strength of a bubble is close to half of that of a SFT, the higher hardening of the He-implanted Cu being due to the larger bubble density.
- Creep deformation takes place only under ion beam irradiation, following a power law with a stress exponent close to 4 with the He-implanted Cu specimen exhibiting lower creep rates for the same applied stress. This lower creep rate is rationalized by a simple strength-based model. The creep behavior under irradiation of both pristine Cu and He-implanted Cu is fully captured by normalizing the stress by the yield stress as dictated by the pre-irradiation or He-implantation,
- The high stress exponent and the dependence on yield stress indicates that the active deformation mechanism is mainly dislocation glide. Dislocation glide is enhanced by irradiation thanks to climb due to the high concentration of point defects or most probably due to the direct dislocation unpinning from obstacles by displacement cascades.

### CRediT authorship contribution statement

**Nargisse Khiara:** Visualization, Validation, Methodology, Investigation, Formal analysis, Data curation. **Michaël Coulombier:** Writing – review & editing, Validation, Resources, Investigation, Data curation, Conceptualization. **Jean-Pierre Raskin:** Writing – review & editing, Supervision, Resources, Funding acquisition, Conceptualization. **Yves Bréchet:** Writing – review & editing, Supervision, Conceptualization. **Thomas Pardoen:** Writing – review & editing, Writing – original draft, Validation, Supervision, Methodology, Funding acquisition, Conceptualization. **Fabien Onimus:** Writing – review & editing, Writing – original draft, Validation, Supervision, Methodology, Investigation, Funding acquisition, Conceptualization.

### Declaration of competing interest

The authors declare that they have no known competing financial interests or personal relationships that could have appeared to influence the work reported in this paper.

### Acknowledgments

The authors want to thank the IJCLab/MOSAIC team, Jérôme Bourçois, Sandrine Picard, and Cyril Bachelet, for the ion irradiation experiments. The authors are grateful to Elodie Rouesne and Amélie Gangloff for SEM operation. Concerning FIB thin foil fabrication, the authors would like to thank Benoit Arnal and the assistance from the "Agence Nationale de la Recherche" program GENESIS referenced as ANR-11-EQPX-0020. The support of the WINFAB platform at UCLouvain is gratefully acknowledged.

### References

[1] J.R. Matthews, M.W. Finnis, Irradiation creep models — An overview, J. Nuclear Mater. 159 (1988) 257-285, https://doi.org/10.1016/0022-3115(88)90097-9, oct.
[2] F. Onimus, T. Jourdan, C. Xu, A.A. Campbell, M. Griffiths, *Irradiation creep in Materials*, Konings, R., Stoller, R. E. Eds., vol. Vol. 1. in Comprehensive Nuclear Materials, Second Edition, vol. Vol. 1. Elsevier Ltd, 2020. [En ligne]. Disponible sur: https://doi.org/10.1016/b978-0-12-803581-8.11645-5.
[3] R.B. Adamson, C.E. Coleman, M. Griffiths, Irradiation creep and growth of zirconium alloys: A critical review, J. Nuclear Mater. 521 (2019) 167-244, https://doi.org/10.1016/j.jnucmat.2019.04.021, août.
[4] D.R. Harries, Irradiation creep in non-fissile metals and alloys, J. Nuclear Mater. 65 (1977) 157-173, https://doi.org/10.1016/0022-3115(77)90052-6, mars.
[5] P. Jung, A. Schwarz, H.K. Sahu, An apparatus for applying tensile, compressive and cyclic stresses on foil specimens during light ion irradiation, Nucl Inst Methods Phys. Res. Section A: Accel., Spectromet. Detectors Assoc. Equ. 234 (2) (1985) 331-334, https://doi.org/10.1016/0168-9002(85)90925-8, févr.
[6] J. Chen, P. Jung, M.A. Pouchon, T. Rebac, W. Hoffelner, Irradiation creep and precipitation in a ferritic ODS steel under helium implantation, J. Nuclear Mater. 373 (1-3) (2008) 22-27, https://doi.org/10.1016/j.jnucmat.2007.04.051, févr.
[7] J. Chen, W. Hoffelner, Irradiation creep of oxide dispersion strengthened (ODS) steels for advanced nuclear applications, J. Nuclear Mater. 392 (2) (2009) 360-363, https://doi.org/10.1016/j.jnucmat.2009.03.025, juill.
[8] J. Chen, et al., Helium effects on creep properties of Fe–14CrWTi ODS steel at 650°C, J. Nuclear Mater. 453 (1-3) (2014) 253-258, https://doi.org/10.1016/j.jnucmat.2014.07.010, oct.
[9] C. Xu, G.S. Was, In situ proton irradiation creep of ferritic–martensitic steel T91, J. Nuclear Mater. 441 (1-3) (2013) 681-687, https://doi.org/10.1016/j.jnucmat.2013.03.046, oct.
[10] B. Moore, M. Topping, R. Guo, T. Feuerstake, C. McDonald, M.R. Daymond, The design and implementation of an in-situ mechanical loading apparatus used during proton-irradiations, J. Nuclear Mater. 583 (2023) 154529, https://doi.org/10.1016/j.jnucmat.2023.154529 sept.
[11] S. Özerinç, R.S. Averback, W.P. King, In situ creep measurements on micropillar samples during heavy ion irradiation, J. Nuclear Mater. 451 (1-3) (2014) 104-110, https://doi.org/10.1016/j.jnucmat.2014.03.037, août.
[12] S. Özerinç, H.J. Kim, R.S. Averback, W.P. King, Direct measurements of irradiation-induced creep in micropillars of amorphous Cu56Ti38Ag6, Zr52Ni48, Si, and SiO2, J. Appl. Phys. 117 (2) (2015), https://doi.org/10.1063/1.4905019 janv.
[13] S.J. Dillon, et al., Irradiation-induced creep in metallic nanolaminates characterized by In situ TEM pillar nanocompression, J. Nuclear Mater. 490 (2017) 59-65, https://doi.org/10.1016/j.jnucmat.2017.04.008, juill.
[14] G.S. Jawaharram, P.M. Price, C.M. Barr, K. Hattar, R.S. Averback, S.J. Dillon, High temperature irradiation induced creep in Ag nanopillars measured via in situ transmission electron microscopy, Scr. Mater. 148 (2018) 1-4, https://doi.org/10.1016/j.scriptamat.2018.01.007.
[15] G.S. Jawaharram, C.M. Barr, A.M. Monterrosa, K. Hattar, R.S. Averback, S. J. Dillon, Irradiation induced creep in nanocrystalline high entropy alloys, Acta Mater. 182 (2020) 68-76, https://doi.org/10.1016/j.actamat.2019.10.022, janv.

[16] K. Tai, R.S. Averback, P. Bellon, Y. Ashkenazy, Irradiation-induced creep in nanostructured Cu alloys, Scr. Mater. 65 (2) (2011) 163-166, https://doi.org/10.1016/j.scriptamat.2011.04.001, juill.

[17] K. Tai, R.S. Averback, P. Bellon, Y. Ashkenazy, B. Stumphy, Temperature dependence of irradiation-induced creep in dilute nanostructured Cu–W alloys, J. Nuclear Mater. 422 (1-3) (2012) 8-13, https://doi.org/10.1016/j.jnucmat.2011.11.068, mars.

[18] P. Lapouge, F. Onimus, R. Vayrette, J.-P. Raskin, T. Pardoen, Y. Bréchet, A novel on chip test method to characterize the creep behavior of metallic layers under heavy ion irradiation, J. Nuclear Mater. 476 (2016) 20-29, https://doi.org/10.1016/j.jnucmat.2016.04.014, août.

[19] P. Lapouge, F. Onimus, M. Coulombier, J.-P. Raskin, T. Pardoen, Y. Bréchet, Creep behavior of submicron copper films under irradiation, Acta Mater. 131 (2017) 77-87, https://doi.org/10.1016/j.actamat.2017.03.056, juin.

[20] M.L. Grossbeck, J.A. Horak, Irradiation creep in type 316 stainless steel and us PCA with fusion reactor He/dpa levels, J. Nuclear Mater. 155-157 (1988) 1001-1005, https://doi.org/10.1016/0022-3115(88)90457-6, juill.

[21] M.L. Grossbeck, K. Ehrlich, C. Wassilew, An assessment of tensile, irradiation creep, creep rupture, and fatigue behavior in austenitic stainless steels with emphasis on spectral effects, J. Nuclear Mater. 174 (2-3) (1990) 264-281, https://doi.org/10.1016/0022-3115(90)90240-n, nov.

[22] F.A. Garner, M.B. Toloczko, M.L. Grossbeck, The dependence of irradiation creep in austenitic alloys on displacement rate and helium to dpa ratio, J. Nuclear Mater. 258-263 (1998) 1718-1724, https://doi.org/10.1016/s0022-3115(98)00227-x, oct.

[23] C.H. Woo, F.A. Garner, Contribution to irradiation creep arising from gas-driven bubble growth, J. Nuclear Mater. 271-272 (1999) 78-83, https://doi.org/10.1016/s0022-3115(98)00731-4, mai.

[24] T. Atkins, R.J. McElroy, Development of fusion first-wall radiation damage facilities, J. Nuclear Mater. 155-157 (1988) 1325-1327, https://doi.org/10.1016/0022-3115(88)90520-x, juill.

[25] M. Li et S. J. Zinkle, Radiation effects in copper and copper alloys for fusion applications, Comprehens. Nuclear Mater. (2020) 93-113, https://doi.org/10.1016/b978-0-12-803581-8.11618-2.

[26] S. Gravier, et al., New on-chip nanomechanical testing laboratory - applications to aluminum and polysilicon thin films, J. Microelectromech. Syst. 18 (3) (2009) 555-569, https://doi.org/10.1109/jmems.2009.2020380, juin.

[27] M. Coulombier, G. Guisbiers, M.-S. Colla, R. Vayrette, J.-P. Raskin, T. Pardoen, On-chip stress relaxation testing method for freestanding thin film materials, Rev. Sci. Inst. 83 (10) (2012), https://doi.org/10.1063/1.4758288 oct.

[28] R. Vayrette, J.-P. Raskin, et T. Pardoen, On-chip fracture testing of freestanding nanoscale materials, Eng. Fract. Mech. 150 (2015) 222-238, https://doi.org/10.1016/j.engfracmech.2015.07.006, déc.

[29] T. Pardoen, et al., A versatile lab-on-chip test platform to characterize elementary deformation mechanisms and electromechanical couplings in nanoscopic objects, *Comptes Rendus. Phys.* 17 (3-4) (2015) 485-495, https://doi.org/10.1016/j.crhy.2015.11.005, nov.

[30] M.S. Colla, B. Amin-Ahmadi, H. Idrissi, L. Malet, S. Godet, J.P. Raskin, D. Schryvers, T. Pardoen, Dislocation mediated relaxation in nanograined columnar palladium films revealed by on-chip time-resolved HRTEM testing, Nature Commun. 6 (2015) 5922, https://doi.org/10.1038/ncomms6922.

[31] J.F. Ziegler, M.D. Ziegler, J.P. Biersack, SRIM – The stopping and range of ions in matter, Nuclear Inst. Methods Phys. Res. Sect. B: Beam Int. Mater. Atoms 268 (11-12) (2010) 1818-1823, https://doi.org/10.1016/j.nimb.2010.02.091.

[32] R.E. Stoller, M.B. Toloczko, G.S. Was, A.G. Certain, S. Dwaraknath, F.A. Garner, On the use of SRIM for computing radiation damage exposure, Nuclear Inst. Methods Phys. Res. Sect. B: Beam Int. Mater. Atoms 310 (2013) 75-80, https://doi.org/10.1016/j.nimb.2013.05.008, sept.

[33] S. Agarwal, Y. Lin, C. Li, R. Stoller, S. Zinkle, On the use of SRIM for calculating vacancy production: quick calculation and full-cascade options, Nuclear Inst. Methods Phys. Res. Sect. B: Beam Int. Mater. Atoms 503 (2021) 11-29.

[34] W. Phythian, R. Stoller, A. Foreman, A. Calder, D. Bacon, A comparison of displacement cascades in copper and iron by molecular dynamics and its application to microstructural evolution, J. Nuclear Mater. 223 (3) (1995) 245-261.

[35] ASTM, Standard practice for neutron radiation damage simulation by charged-particle irradiation. *ASTM E521, Annual Book of ASTM Standards*, American Society of Testing and Materials., Philadelphia, 1994 vol. 12.02.

[36] J. Corbett, J. Denney, M. Fiske, R. Walker, Electron irradiation of copper near 10 K, Phys. Rev. 108 (4) (1957) 954.

[37] W. Bauer, A. Sosin, Threshold displacement energies and subthreshold displacements in copper and gold near 10° K, J. Appl. Phys. 35 (3) (1964) 703-709.

[38] Y. Yang, D. Frazer, M. Balooch, P. Hosemann, Irradiation damage investigation of helium implanted polycrystalline copper, J. Nuclear Mater. 512 (2018) 137-143.

[39] J.-P. Crocombette, C. Van Wambeke, Quick calculation of damage for ion irradiation: implementation in Iradina and comparisons to SRIM, EPJ N-Nuclear Sci. Technol. 5 (2019) 7.

[40] E.S. Aitkhozhin, E.V. Chumakov, Radiation-induced creep of copper, aluminium and their alloys, J. Nuclear Mater. 233-237 (1996) 537-541, https://doi.org/10.1016/s0022-3115(96)00291-7, oct.

[41] P. Jung, Irradiation creep of 20% cold-worked copper, J. Nuclear Mater.s 200 (1) (1993) 138-140, https://doi.org/10.1016/0022-3115(93)90017-s, mars.

[42] U. Kocks, A.S. Argon, M.F. Ashby, Thermodynamics and Kinetics of Slip 19 (1975) 231-234.

[43] D. Caillard, J. Martin, Thermally Activated Mechanisms in Crystal Plasticity, 8, Pergamon Materials Series, Pergamon, 2003.

[44] U. Kocks, Constitutive behavior based on crystal plasticity. Unified Constitutive Equations For Creep and Plasticity, Springer, 1987, p. 1-88.

[45] J. Gittus, Creep, Viscoelasticity and Creep Fracture in Solids, Elseviers Applied Science Publishers, London, 1975.

[46] M.E. Kassner, Fundamentals of Creep in Metals and Alloys, Butterworth-Heinemann, 2015.

[47] M.L. Jenkins, M.A. Kirk, Characterisation of Radiation Damage By Transmission Electron Microscopy, CRC Press, 2000.

[48] Q.M. Wei, N. Li, N. Mara, M. Nastasi, A. Misra, Suppression of irradiation hardening in nanoscale V/Ag multilayers, Acta Mater. 59 (16) (2011) 6331-6340, https://doi.org/10.1016/j.actamat.2011.06.043, sept.

[49] Q. Guo, P. Landau, P. Hosemann, Y. Wang, J.R. Greer, Helium implantation effects on the compressive response of Cu nanopillars, Small. 9 (5) (2012) 691-696, https://doi.org/10.1002/smll.201201614, nov.

[50] Z.-J. Wang, F.I. Allen, Z.-W. Shan, P. Hosemann, Mechanical behavior of copper containing a gas-bubble superlattice, Acta Mater. 121 (2016) 78-84, https://doi.org/10.1016/j.actamat.2016.08.085, déc.

[51] N. Li, M. Nastasi, A. Misra, Defect structures and hardening mechanisms in high dose helium ion implanted Cu and Cu/Nb multilayer thin films, Int. J. Plast. 32-33 (2012) 1-16, https://doi.org/10.1016/j.ijplas.2011.12.007, mai.

[52] D. Kiener, P. Hosemann, S.A. Maloy, A.M. Minor, In situ nanocompression testing of irradiated copper, Nat. Mater. 10 (8) (2011) 608-613, https://doi.org/10.1038/nmat3055, juin.

[53] S.J. Zinkle, L.L. Snead, Microstructure of copper and nickel irradiated with fission neutrons near 230°C, J. Nuclear Mater. 225 (1995) 123-131, https://doi.org/10.1016/0022-3115(94)00670-9, août.

[54] B.N. Singh, D.J. Edwards, P. Toft, Effect of neutron irradiation and post-irradiation annealing on microstructure and mechanical properties of OFHC-copper, J. Nuclear Mater. 299 (3) (2001) 205-218, https://doi.org/10.1016/s0022-3115(01)00698-5, déc.

[55] R. Schäublin, Z. Yao, P. Spätig, M. Victoria, Dislocation defect interaction in irradiated Cu, Mater. Sci. Eng. A 400-401 (2005) 251-255, https://doi.org/10.1016/j.msea.2005.03.093, juill.

[56] R. Schäublin, Z. Yao, P. Spätig, M. Victoria, Dislocation defect interaction in irradiated Cu, Mater. Sci. Eng. A 400-401 (2005) 251-255, https://doi.org/10.1016/j.msea.2005.03.093, juill.

[57] J. Marian, E. Martínez, H.-J. Lee, B.D. Wirth, Micro/meso-scale computational study of dislocation-stacking-fault tetrahedron interactions in copper, J. Mater. Res. 24 (12) (2009) 3628-3635.

[58] Y.N. Osetsky, D.J. Bacon, Atomic-scale mechanisms of void hardening in bcc and fcc metals, Philosoph. Mag. 90 (7-8) (2010) 945-961.

[59] L. Tan et J. T. Busby, Formulating the strength factor α for improved predictability of radiation hardening, J. Nuclear Mater. 465 (2015) 724-730.

[60] D. Bacon, U. Kocks, R. Scattergood, The effect of dislocation self-interaction on the Orowan stress, Philosoph. Mag. 28 (6) (1973) 1241-1263.

[61] C. Sobie, N. Bertin, L. Capolungo, Analysis of obstacle hardening models using dislocation dynamics: application to irradiation-induced defects, Metallurgical and Materials Trans. A 46 (8) (2015) 3761-3772.

[62] R. Scattergood, D. Bacon, The strengthening effect of voids, Acta Metallurg. 30 (8) (1982) 1665-1677.

[63] Y. Xiang, T. Tsui, J.J. Vlassak, The mechanical properties of freestanding electroplated Cu thin films, J. Mater. Res. 21 (6) (2006) 1607-1618.

[64] T. Pardoen, Size and rate dependent necking in thin metallic films, J. Mech. Phys. Solids. 62 (2014) 81-98.

[65] P.T. Heald, M.V. Speight, Steady-state irradiation creep, Philosoph. Mag. 29 (5) (1974) 1075-1080, https://doi.org/10.1080/14786437408226592, mai.

[66] R. Bullough, J.R. Willis, The stress-induced point defect-dislocation interaction and its relevance to irradiation creep, Philosoph. Mag. 31 (4) (1975) 855-861, https://doi.org/10.1080/14786437508229635, avr.

[67] W.G. Wolfer, M. Ashkin, Diffusion of vacancies and interstitials to edge dislocations, J. Appl. Phys. 47 (3) (1976) 791-800, https://doi.org/10.1063/1.322710, mars.

[68] C. Woo, E. Savino, Stress-induced preferred absorption due to saddle-point anisotropy: the case of an infinitesimal dislocation loop, J. Nuclear Mater.s 116 (1) (1983) 17-28.

[69] A. Brailsford, R. Bullough, Irradiation creep due to the growth of interstitial loops, Philosoph. Mag. 27 (1) (1973) 49-64.

[70] F.A. Garner, D.S. Gelles, Irradiation creep mechanisms: an experimental perspective, J. Nuclear Mater.s 159 (1988) 286-309, https://doi.org/10.1016/0022-3115(88)90098-0, oct.

[71] D.Da Fonseca, F. Mompiou, T. Jourdan, J.-P. Crocombette, A. Chartier, F. Onimus, Evidence of dislocation loop preferential nucleation in irradiated aluminum under stress, Scr. Mater. 233 (2023) 115510, https://doi.org/10.1016/j.scriptamat.2023.115510 août.

[72] J.H. Gittus, Theory of dislocation-creep due to the frenkel defects or interstitialcies produced by bombardment with energetic particles, Philosoph. Mag. 25 (2) (1972) 345-354, https://doi.org/10.1080/14786437208226809, févr.

[73] N. Khiara, et al., In-situ TEM irradiation creep experiment revealing radiation induced dislocation glide in pure copper, Acta Mater. 216 (2021) 117096, https://doi.org/10.1016/j.actamat.2021.117096 sept.

[74] M. Gaumé, P. Baldo, F. Mompiou, F. Onimus, In-situ observation of an irradiation creep deformation mechanism in zirconium alloys, Scr. Mater. 154 (2018) 87-91.

[75] N. Khiara, et al., A novel displacement cascade driven irradiation creep mechanism in α-zirconium: A molecular dynamics study, J. Nuclear Mater. 541 (2020) 152336, https://doi.org/10.1016/j.jnucmat.2020.152336 déc.

[76] N. Khiara, et al., A molecular dynamics study of a cascade induced irradiation creep mechanism in pure copper, J. Nuclear Mater. 560 (2022) 153518, https://doi.org/10.1016/j.jnucmat.2022.153518 mars.
[77] S. Li, H. Xie, L. Yu, X. Xiao, A steady-state irradiation creep and thermal creep model for zirconium alloys, Int. J. Plast. 172 (2024) 103814.
[78] P. Jung, Stress and stress transient effects on irradiation creep of 20% cold worked stainless steels and nickel alloys, J. Nuclear Mater. 113 (2-3) (1983) 133-141, https://doi.org/10.1016/0022-3115(83)90135-6, janv.
[79] P. Jung, M.I. Ansari, A correlation between irradiation creep strength and yield stress of FCC metals and alloys, J. Nuclear Mater. 138 (1) (1986) 40-45, https://doi.org/10.1016/0022-3115(86)90253-9, mars.
[80] J. Nagakawa, V.K. Sethi, A.P.L. Turner, Irradiation creep in simple binary alloys, J. Nuclear Mater. 104 (1981) 1275-1279, https://doi.org/10.1016/0022-3115(82)90777-2, janv.
[81] B.N. Singh, S.J. Zinkle, Defect accumulation in pure fcc metals in the transient regime: a review, J. Nuclear Mater. 206 (2-3) (1993) 212-229, https://doi.org/10.1016/0022-3115(93)90125-i, nov.